*Journal of Structural Geology*, Vol. 10, No. 3, pp. 249 to 262, 1988
Printed in Great Britain

0191-8141/88 $03.00 + 0.00


# Quasistatic propagation of a normal fault: a fracture mechanics model

JIAN LIN and E. M. PARMENTIER

Department of Geological Sciences, Brown University, Providence, RI 02912, U.S.A.

(*Received* 26 *February* 1987; *accepted in revised form* 15 *September* 1987)

**Abstract**—We have carried out boundary element calculations to simulate quasistatic propagation of a normal fault in the earth's crust under a horizontal tensile loading. Byerlee's frictional law is employed to describe the mechanical behavior of the fault surface. We hypothesize that in order for a normal fault to grow quasistatically, the mixed-mode effective shear stress intensity factor must exceed a threshold value (fracture toughness), a crustal material property. We suggest that the fault grows in a direction of local maximum shear stress. The direction of fault propagation thus depends on the ratio of tensile and shear stress intensity factors. A listric normal fault is likely to form in crustal material with a small shear fracture toughness. A listric normal fault is also more likely to form in crustal material with a high degree of plasticity.

The propagation trajectory of an incrementally growing normal fault is examined. As the normal fault extends to a greater depth, the shear stress intensity factor drops, owing to an increase in fault surface friction. The equilibrium depth to which a normal fault will grow is controlled by the far field loading and the fracture mechanical property of the crustal material. The decrease of shear stress intensity with fault length also stabilizes the fault growth.

## INTRODUCTION

EXTENSIONAL tectonic domains exhibit normal faulting and block tilting at upper levels in the crust. These extensional structures include (1) continental rifts, which are generally considered to be early stages of stretching in the continental crust, (2) continental margins, as a stage following the previous, (3) oceanic rifts and plate accretion zones on ocean ridges and (4) large continental areas such as the Basin and Range Province and Tibetan Plateau (Brun & Choukroune 1983, Jackson & McKenzie 1983).

One of the early attempts to apply mechanics to the faulting process was Anderson's theory of faulting (1951). Taking the Coulomb–Navier and Mohr criteria for shear fracture, Anderson interpreted normal, thrust and strike-slip faults in terms of the magnitudes of the horizontal principal stresses relative to that of the vertical principal stress. Faulting is predicted to occur on planes in which resultant shear stress exceeds frictional resistance. Anderson's simple classification ignores the effect of stress-gradients, which must certainly exist in the earth, especially in the vertical direction.

Hafner (1951) used simple polynomial solutions of the stress equilibrium equations to obtain the stress trajectories in a block under both horizontal compression and shearing. He proposed that if the Mohr–Coulomb failure criterion is satisfied at a point in the block, fracture will take place on a local plane in which shear stress exceeds frictional resistance. Furthermore, Hafner constructed a family of curves intersecting these local planes and interpreted them as the locations of potential fault surfaces. The limitation of this approach is that once a fracture has occurred, the stress trajectories inferred from simple polynomial solutions cease to be valid. Instead of plotting directions of potential fracture surface, Sanford (1959) gives contours of the strain energy of distortion to indicate the region in which failure is most likely to occur.

Berg (1965) studied the deformation of a narrow elliptical crack (with geometric aspect ratio of $b/a$) in an elastic body loaded first by high hydrostatic pressure (which squeezes the crack shut) and then by shear stresses (which tend to slide the crack surfaces across each other). He found that the closing of the crack is determined only by the component of compressive stress normal to the crack; the compressive stress required to close the crack of aspect ratio $b/a$ lying in a material having shear modulus $G$ and Poisson's ratio $\nu$ is $Gb/a(1 - \nu)$. Since lithostatic stress in the earth's crust increases linearly with depth, we expect a crack to be closed at great depth.

Digby & Murrell (1975) investigated the shear stresses along a fault boundary and discussed the effect of ductility on faulting in terms of the material response to tensile and shearing stresses. They also approximated a fault segment to an ellipsoidal cavity within an elastic matrix. For an elastic solid they found that fracture is initiated at the leading and trailing edges of the fault. At higher stresses fracture spreads around the fault periphery when one or more principal stresses are tensile. However, when the applied stresses are all compressive, failure will be by a local shear mechanism. Considering an elastic body in which short segments of cracks are randomly distributed but sufficiently far away that the stress field on a crack is not perturbed by the presence of other cracks, Digby & Murrell (1975) found that the greatest shear stress occurs on cracks making an angle $\psi$ with the major principal applied stress axis, where $\tan(2\psi) = 1/\mu_f$; $\mu_f$ being the friction coefficient at the fault surface. This orientation is consistent with the faulting direction predicted by Anderson's theory (1951).

Fracture mechanics concerns the study of stress con-

centrations caused by sharp-ended flaws and the conditions for the propagation of these flaws. Although this approach has been very successful at explaining many features of the brittle and ductile failure of engineering materials under tensile loads, its application to geological materials has not been widespread because of a historical preference for dislocation theory. In the dislocation approach, the relative motion on the surface of a discontinuity is assumed *a priori*, whereas in fracture mechanics, a criterion based on plausible physical grounds or experimental evidence is used to determine whether the region of relative displacement will spread. The usefulness of the fracture mechanics approach is largely due to the success of simple fracture criteria in describing the failure of many materials. An extensive review of theoretical studies on shear band propagation and its application to earthquake studies can be found in Rudnicki (1980).

In this paper we examine the formation of a normal fault by the progressive growth of a shear crack in the earth's crust. Tectonic tensile stresses at the boundaries of a geological domain cause the stress concentrations at the end of a pre-existing weakness (crack). We will analyse the stress distribution at the crack tip and predict its growth using fracture mechanics criteria.

It is well known that across currently active faults, shear displacements generally take place either by intermittent seismic failure or by aseismic fault creep (Scholz *et al.* 1969). Even in the case of aseismic motion, two situations may arise: either stable sliding occurs at constant load, or transient slip takes place accompanied by a partial release of stress, giving rise to a stick–slip oscillation (Jaeger & Cook 1969). Dynamic shear cracks have been investigated as models for earthquake mechanisms (Freund 1979, Das & Scholz 1981). In this study we will only consider a normal fault which grows at a speed much lower than the elastic wave velocities. In this case, the kinetic energy is relatively insignificant compared to the potential energy of the loading arrangement and the strain energy of the elastic medium. The system can be regarded as quasistatic, in so far as the static solutions describe the critical requirements for crack extension to sufficient accuracy.

One important aspect of this paper is to study the relationship between planar and listric normal faulting. Despite the common occurrence of planar normal faults, the dip of many high angle normal faults appears to decrease with depth (listric normal fault). Examples of listric normal faults have been described in the continental extensional environments, such as the Basin and Range Province in the western United States (Proffett 1977, Effimoff & Pinezich 1981, Anderson *et al.* 1983). Recently, Karson (1984) and Harper (1985) proposed that listric normal faults may also occur in oceanic extensional domains, such as the accretion zone at mid-ocean ridges. Listric normal faults as revealed by seismic reflection profiles have also been found in continental margins (cf. Wernicke & Burchfiel 1982).

Although many mechanisms based on kinematic and crustal rheology arguments have been proposed to explain listric normal faults (e.g. Wernicke & Burchfiel 1982, Jackson & McKenzie 1983), to our knowledge, no self-consistent mechanical models have been proposed. We will address this question by examining the propagation direction of a quasistatic normal fault. As will be shown later by fracture mechanics analysis, the pattern of fault growth is controlled by the ratio of shear and tensile stress intensity factors.

## FRACTURE MECHANICS MODEL FOR NORMAL FAULTS

Our model of a normal fault is shown schematically in Fig. 1. Initially we have a weakness (crack) inclined at an angle $\psi$ to the free surface of the elastic half space. The end of the crack is at a depth $H$. Prior to the tectonic loading at the boundaries of the domain under consideration, only lithostatic stresses act across the crack surface. Therefore the crack surfaces are in contact, and neither tensile nor shear displacements occur. As shown in Fig. 1, the lithostatic stress increases linearly with depth. In the following, we will consider a case where angle $\psi$ is 60°.

The loading on the boundaries of the geological domain under consideration is presumed to be of tectonic origin. Since it is not clear how the tensile stress is distributed with depth in a specific tectonic environment, we will consider two plausible examples: one in which the far field tensile stress is independent of depth (as shown in Fig. 1), and a second in which the tensile stress increases linearly with depth.

Displacement–discontinuity boundary element methods have proved very useful for analysing crack problems (Mills 1981, Cornet 1979, Crouch & Starfield 1983). In this method, a singular solution is first integrated to find the Green's function for a particular dislocation distribution over a line segment; for example, constant, linear variation or square root variation could be employed. These Green's functions are

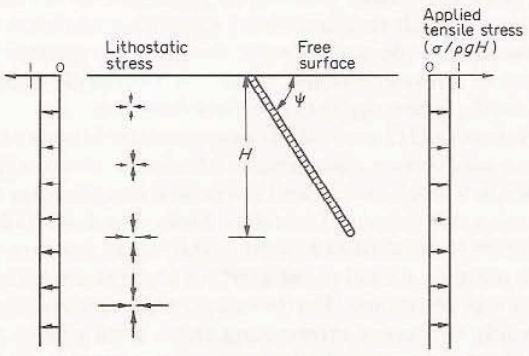


Fig. 1. A two-dimensional mechanical model of a normal fault in an elastic half-plane. Initially, a pre-existing crack (weakness) is inclined at an angle $\psi$ to the free surface. The domain under consideration is initially under lithostatic stress. The surface of the crack deforms in response to a far field tensile loading. The crack is discretized into $N$ boundary elements, for each of which displacements and stresses are represented by the values at the mid-point of the element.

then used to produce a system of simultaneous equations involving only boundary conditions. Boundary element methods reduce the problem dimensionality by one and require discretization only along the boundaries of the domain under consideration as opposed to the finite difference or finite element techniques which necessitate that the entire domain be discretized.

As shown in Fig. 1 we discretize the crack (fault) into a finite number ($N$) of boundary line segments or elements, within which the shear and normal tractions ($\boldsymbol{\sigma}_s$ and $\boldsymbol{\sigma}_n$) are continuous across the fault surface, but in which the shear and normal displacements ($\mathbf{u}_s$ and $\mathbf{u}_n$) may be discontinuous. We denote the displacement-discontinuities as $\mathbf{D}_s = \mathbf{u}_s^+ - \mathbf{u}_s^-$ and $\mathbf{D}_n = \mathbf{u}_n^+ - \mathbf{u}_n^-$ where the terms with + and − superscripts represent displacements on the top and bottom of the normal fault respectively. The stresses and displacements caused by a displacement-discontinuity on a fault element must be analytically evaluated. For an element in an elastic half plane with a stress free surface and under plane strain conditions, we have developed the exact solutions (Green's functions) for the cases when displacement-discontinuity is constant along the element and when it varies as a square root function of the distance from one end. The latter solution is useful in representing the fault tip element, where it has been found that relative displacements on fault surface increase as a square root function of the distance away from the tip (Rice 1968, Mills 1981). The derivation of Green's functions and other related formulae are given in the Appendix. Finally, these solutions are combined to construct solutions to the given boundary-value problem. This creates a set of linear equations relating boundary stresses and boundary displacements to a set of displacement-discontinuities. Since our basic analytical solutions (Green's functions) are developed for a semi-infinite region, there is no need to place boundary elements on the free surface. This greatly reduces the number of the linear equations and therefore the computing effort.

The normal and tangential stresses acting at the center of an element on the crack (fault) are related to the displacement-discontinuities $\mathbf{D}$s of all elements by

$$\begin{bmatrix} \boldsymbol{\sigma}_s \\ \boldsymbol{\sigma}_n \end{bmatrix} = \begin{bmatrix} \mathbf{A}_{ss} & \mathbf{A}_{sn} \\ \mathbf{A}_{ns} & \mathbf{A}_{nn} \end{bmatrix} \begin{bmatrix} \mathbf{D}_s \\ \mathbf{D}_n \end{bmatrix}, \tag{1a}$$

where the $\mathbf{A}$s are $N$ by $N$ submatrices and $\boldsymbol{\sigma}_s$, $\boldsymbol{\sigma}_n$, $\mathbf{D}_s$ and $\mathbf{D}_n$ are column vectors of $N$ components. The tangential and normal components of the displacements on the fault are related to the displacement-discontinuities by a similar set of equations

$$\begin{bmatrix} \mathbf{u}_s \\ \mathbf{u}_n \end{bmatrix} = \begin{bmatrix} \mathbf{B}_{ss} & \mathbf{B}_{sn} \\ \mathbf{B}_{ns} & \mathbf{B}_{nn} \end{bmatrix} \begin{bmatrix} \mathbf{D}_s \\ \mathbf{D}_n \end{bmatrix}, \tag{1b}$$

where the $\mathbf{B}$s are $N$ by $N$ submatrices and $\mathbf{u}_s$ and $\mathbf{u}_n$ are column vectors of $N$ components.

The matrices $\mathbf{A}$ and $\mathbf{B}$ depend solely on the geometry of the problem, the type of the elements involved (constant or square root variation), and the material properties. If an additional element is introduced, only one row and one column have to be added to the previous submatrices; all the other coefficients remain unchanged.

Once the coordinates and the boundary conditions of the $N$ elements on the crack (fault) have been defined, the system of $N$ equations can be solved for the unknown displacements-discontinuity $\mathbf{D}_n$ and $\mathbf{D}_s$. The stress state and the displacements at any point of the continuum are then obtained directly from equations similar to (1a) and (1b); this time however the $\mathbf{D}$s are known and the stresses and displacements are computed.

We consider a fault which is filled with thin compressible material (cf. Segall & Pollard 1983). Before inelastic deformations (slip or separation) occur on the fault, the fault surface is in contact and the fault-filling material deforms elastically in response to far field loading. A fault element can then be modeled as a displacement-discontinuity whose opposite surfaces are connected by a spring, with the normal and shear stiffnesses of the spring $\mathbf{C}_n$ and $\mathbf{C}_s$ chosen to be representative of the properties of the fault-filling material. Namely,

$$\begin{aligned} \Delta\boldsymbol{\sigma}_s &= C_s \Delta\mathbf{D}_s \\ \Delta\boldsymbol{\sigma}_n &= C_n \Delta\mathbf{D}_n, \end{aligned} \tag{2}$$

where $\Delta\mathbf{D}_s$ and $\Delta\mathbf{D}_n$ are the incremental elastic deformations of the fault-filling material under incremental loading $\Delta\boldsymbol{\sigma}_s$ and $\Delta\boldsymbol{\sigma}_n$ across the fault element. More discussions on the meaning of $C_s$ and $C_n$ will be given later.

When the frictional sliding envelope of a fault element is reached, the surfaces of this element will either separate or slide, resulting in inelastic deformations. The frictional sliding on a typical element is governed by Byerlee's law

$$|\boldsymbol{\sigma}_s| \leq C_0 + (-\sigma_n) \tan \phi_0, \tag{3}$$

where $C_0$ and $\phi_0$ are the cohesion and angle of friction of the material at the fault surface. For a fault element at a great depth in the earth's crust, the normal stress $\sigma_n$ across it is compressive. For a fault element close to the free surface, however, this stress may become tensile. In this case another failure mode is possible, namely tensile cracking. We introduce a tensile strength, say

$$\sigma_n = T_0 = 0 \tag{4}$$

and allow the element to open whenever $\sigma_n = 0$. In this case, the total normal and shear stresses are zero on that element. The predicted strength envelope based on conditions (3) and (4) is shown in Fig. 2(a) (dashed lines).

The occurrence of slip along a fault must be modeled as an incremental process. The general approach to this problem is described by Crouch & Starfield (1983). In modeling the progressive slippage on the fault surface, the rock matrix is assigned a Young's modulus of $10^4$ MPa and a Poisson's ratio of 0.2. Elastic stiffnesses for fault-filling material are taken as $C_s = C_n = 10^5$ MPa m$^{-1}$; these relatively high values were chosen so that the fault surface deformations would be small in the absence of any slip or separation. Their effects on fault development will be discussed later. The initial state of stress is

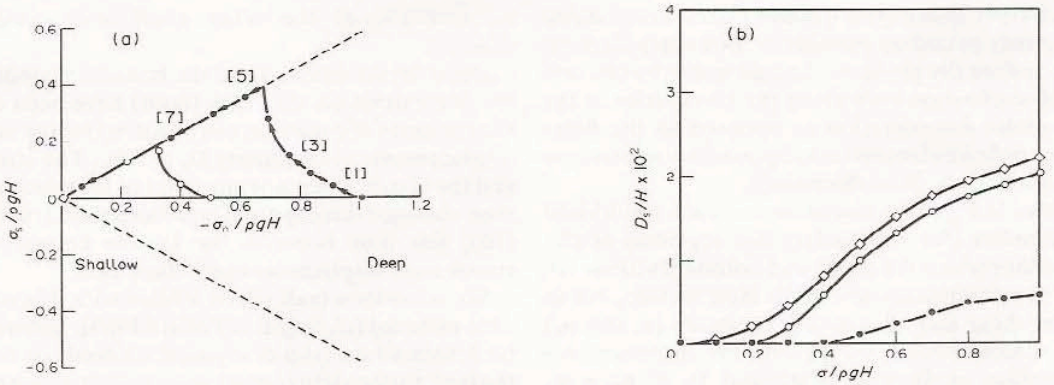


Fig. 2. (a) Stress histories of the selected points on the fault. Filled circle: the element at the fault tip. Open circle: an element at the middle of the fault. Open diamond: the element closest to the free surface. The frictional sliding envelope is shown by the dashed lines. Arrows indicate the directions of the stress change of the fault tip element. (b) Symbols are the same as in (a). Non-dimensional shear displacement-discontinuity is plotted against non-dimensional far field loading. A sharp increase in displacement-discontinuity indicates the beginning of non-elastic deformation.

$$\sigma^0_{xx} = \sigma^0_{zz} = -\varrho gz. \tag{5}$$

The progressive extension of the domain under consideration is simulated by increasing the boundary tensile stress in increments. The behavior of the fault elements from one increment to the next can be shown clearly on the plot of normal and shear stresses on fault surface, as shown in Fig. 2(a). Here, the shear stresses at fault elements are plotted against the corresponding normal (compressive) stresses. The dashed inclined straight lines in the diagram represent the yield conditions (3) and (4); in this example the line passes through the origin because the fault surface material has no cohesion. The circles refer to the increment, or step, and the arrows represent the directions of the changing stress conditions across the fault from one step to the next.

Thus in Fig. 2(a) we see that prior to the application of far field stress, the shear stresses at all elements are zero, and the normal stresses are equal to the lithostatic stress. During the first increment, the normal compressive stress at the fault tip element is reduced and the magnitude of the shear stress increases, as shown by the first arrow. This trend continues until half way between step [4] and step [5], when the yield condition is reached and slip occurs. Further slip takes place during step [5] to step [10]. A similar stress history is observed for the element at the middle of the fault. The surface element behaves differently, because immediately after the far field loading, it opens and the stresses vanish.

The shear displacement-discontinuities of the selected elements at various increments are shown in Fig. 2(b). At the fault tip element no significant shear displacement occurs until after increment [4] at which the strength envelope of the element is reached (compare with Fig. 2a). It can also be observed that the surface element slips at a relatively low far field stress, and the increase in far field loading causes the slip on the fault surface to migrate downward.

In developing the analytic Green's function for fault tip element (see Appendix), we have assumed that both relative shear and normal displacements increase as a square root function of the distance from the fault end, namely

$$\mathbf{u}^+_s - \mathbf{u}^-_s = \mathbf{D}_s(r/a)^{1/2} \tag{6}$$
$$\mathbf{u}^+_n - \mathbf{u}^-_n = \mathbf{D}_n(r/a)^{1/2}, \tag{7}$$

where $a$ is the length of the fault tip element, and $r$ is the distance from the fault end. From the fracture mechanics analysis (Rice 1968), if the shear and normal stress intensity factors for a crack are $K_{II}$ and $K_I$ the relative crack surface displacements will be

$$\mathbf{u}^+_s - \mathbf{u}^-_s = 4(1-\nu)K_{II}(r/2\pi)^{1/2}/G \tag{8}$$
$$\mathbf{u}^+_n - \mathbf{u}^-_n = 4(1-\nu)K_I(r/2\pi)^{1/2}/G. \tag{9}$$

Therefore we obtain the stress intensity factors:

$$K_I = [G/4\pi(1-\nu)](2\pi/a)^{1/2}\mathbf{D}_n \tag{10}$$
$$K_{II} = [G/4\pi(1-\nu)](2\pi/a)^{1/2}\mathbf{D}_s, \tag{11}$$

where $G$ is shear modulus and $\nu$ is Poisson's ratio. $K_I$ and $K_{II}$ thus calculated are plotted in Fig. 3 for the cases when the loading is independent of depth (Fig. 3a) and when the loading linearly increases with depth (Fig. 3b). In Fig. 3(b) far field loading at the surface is zero. It increases to a value of $\sigma$ at a depth $H$, where $H$ is the depth of the lower end of a pre-existing fault.

## FAILURE CRITERION AND FAULT GROWTH DIRECTION

The purpose of computing stress intensity factors is the determination of fracture initiation and subsequent propagation. According to fundamental fracture mechanics, the elastic stress concentration near the crack tip is characterized by stress intensity factors $K_I$ and $K_{II}$ (Lawn & Wilshaw 1975). More specifically, the stress field inside an annular elastic zone around the tip, omitting the higher order terms, is given by

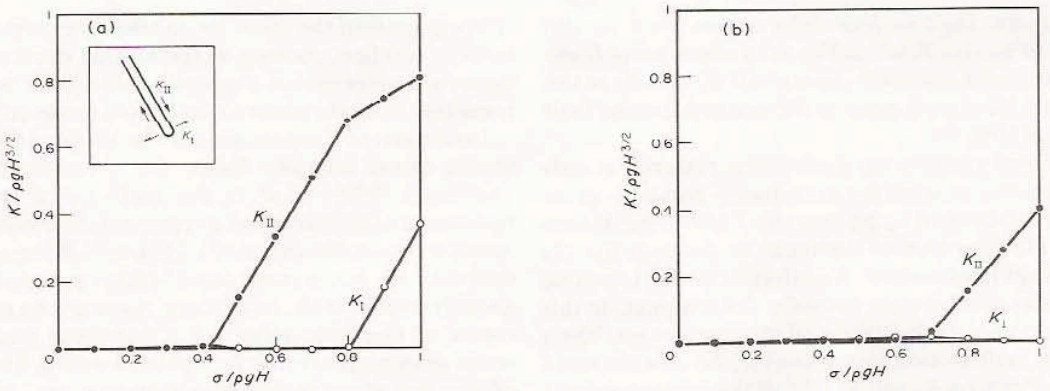


Fig. 3. Inset: $K_I$ characterizes tensile stress and $K_{II}$ characterizes shear stress at the fault tip. (a) Change of $K_I$ and $K_{II}$ as a function of applied loading when the far field loading is independent of depth. Sharp increase in $K_{II}$ indicates the beginning of slip at the fault tip element. Sharp increase of $K_I$ indicates the beginning of tensile opening at the fault tip. $C_s = C_n = 10^5$ MPa m$^{-1}$. (b) Changes of $K_I$ and $K_{II}$ as a function of applied loading when the far field stress increases linearly with depth. $C_s$ and $C_n$ are the same as in (a).

$$\sigma_{rr} = [1/(2\pi r)^{1/2}]\{K_I \cos(\theta/2)[1 + \sin^2(\theta/2)] + K_{II} \sin(\theta/2)[1 - 3\sin^2(\theta/2)]\}$$
$$\sigma_{\theta\theta} = [1/(2\pi r)^{1/2}]\{K_I \cos^3(\theta/2) + K_{II}[-3\sin(\theta/2)]\cos^2(\theta/2)\} \quad (12)$$
$$\sigma_{r\theta} = [1/(2\pi r)^{1/2}]\{K_I \sin(\theta/2)\cos^2(\theta/2) + K_{II}\cos(\theta/2)[1 - 3\sin^2(\theta/2)]\},$$

where $r$ is the distance from the crack tip, and $\theta$ is measured from the crack plane.

From Fig. 3 it is clear that after slip occurs at the fault tip element, the mode II stress intensity factor is much larger than that of mode I. This is a direct consequence of the high lithostatic stress at the fault tip. Because of the high compressive stress, slip occurs at the fault tip element at a stress lower than that for which tensile opening would be possible. Comparison of Fig. 3(a) & (b) reveals that although the exact values of $K_I$ and $K_{II}$ depend on the type of far field loadings, $K_{II}$ dominates $K_I$ in both cases.

In the last section we introduced elastic stiffnesses $C_s$ and $C_n$ for fault-filling material to characterize fault surface deformation prior to inelastic deformation. Inevitably these two parameters are functions of the fault surface conditions, e.g. the roughness of the fault surface and the type of the material filling the fault. Employing a simple one-dimensional stress–strain relationship for compression and shear on an elongate thin elastic element and using the definition of $C_s$ and $C_n$ (equation 2), it can be shown that $C_s = G/h$ and $C_n = E/h$, where $h$ is the thickness of the element and $E$ and $G$ are the Young's modulus and shear modulus for the material making up the element. For a geological fault element, the thicker the material filling the fault the smaller the value of $C_n$ and $C_s$. Large values of $C_s$ and $C_n$ as used in the calculations of Fig. 3 approximate a fault with very little fault-filling material, assuring that fault surface deformation is small in the absence of any inelastic deformation.

To examine the effects of the elastic stiffnesses on the fault motion, we calculated the $K_I$ and $K_{II}$ for two sets of $C_s$ and $C_n$ shown in Fig. 4. In Fig. 4(a), $C_n = 2C_s = 4 \times 10^4$ MPa m$^{-1}$. In Fig. 4(b), $C_n = C_s = 10^4$ MPa m$^{-1}$. Assumed values of $C_s$ and $C_n$ therefore progressively decrease from Fig. 3(a) to Fig. 4(a) and Fig. 4(b). As we

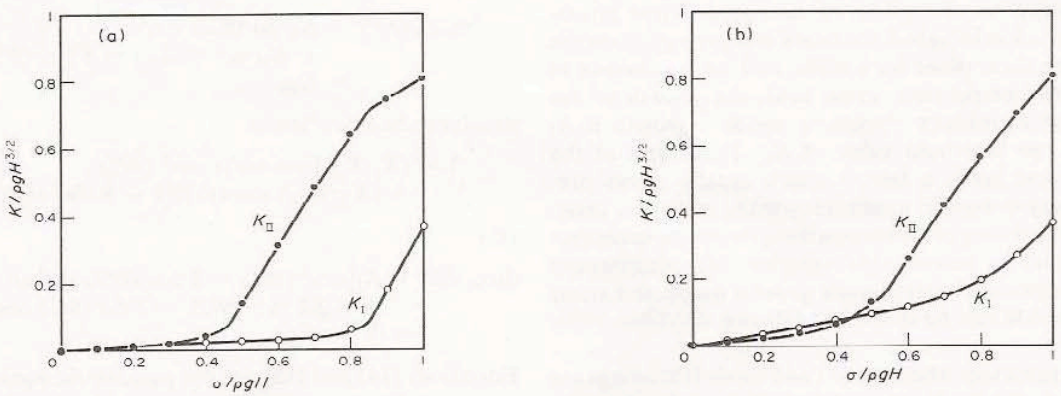


Fig. 4. Change of $K_I$ and $K_{II}$ as a function of applied loading when the far field stress is independent of depth. (a) $C_n = 2C_s = 4 \times 10^4$ MPa m$^{-1}$. They are smaller than those in Fig. 3. (b) $C_s = C_n = 10^4$ MPa m$^{-1}$. They are smaller than those in (a).

would expect, fault surface deformation prior to slip becomes more significant in Fig. 4(b) where more fault-filling material is assumed. As a result $K_I$ and $K_{II}$ at the fault tip are significant prior to slip occurring at the fault tip element (Fig. 4b).

Elastic deformation on fault-filling material is only one of the mechanisms for introducing non-zero stress intensities at the fault tip prior to slip. Other mechanisms include: (1) dilatation of the rocks at the fault tip; (2) roughness of fault surface. An effective normal opening results from smaller scale irregular deformation. In this paper we do not explicitly model these processes. Their effects on fault motion can, however, be characterized by their effects on $K_I$ and $K_{II}$. In all the cases examined below, a fault with small values of $C_s$ and $C_n$ represents the one which has significant $K_I$ and $K_{II}$ before slip occurs at the fault tip element.

The central concept of fracture mechanics, which has its roots in the Griffith energy balance, is that for a crack in an elastic medium, no propagation takes place until the stress intensity factor at the crack tip reaches a value $K_0$ (fracture toughness), a property of the medium. A normal fault is a mode II crack. We can simply define $K_0$ as a threshold value of $K$ below which the crack velocity is vanishingly small and can be neglected.

Most seismic faulting in the earth's crust is thought to involve processes of shear fracture and frictional sliding rather than tensile fracture. In most laboratory experiments, however, shear fractures are unstable in the sense that they tend to propagate out of their original plane (e.g. Ingraffea 1977, Chiu & Liu 1976) thus forming tensile cracks. Nevertheless, several experimental techniques have recently been proposed to measure the critical stress intensity factor for shear fracture in engineering materials (Chisholm & Jones 1977, Agarwal & Giare 1981, Banks-sills *et al.* 1983, Davies *et al.* 1985). Using these techniques, which include high confining pressures and special geometrical constraints, $K_{II}$ at a crack tip can be 10 to 200 times larger than $K_I$, and the out-of plane tensile cracking can be prevented.

Analogously, shear mode growth can be dominant in some fatigue experiments. Liu (1985) pointed out that a fatigue crack is often initiated by localized cyclic plastic deformation on the plane of maximum shear stress. Once a crack is initiated, the crack will propagate on the maximum shear plane for a while, and, in the absence of an overall compressive stress field, the growth of the crack will eventually change to mode I growth if $K_I$ exceeds the threshold value of $K_I$. Therefore, at the macroscopic level, a fatigue crack usually grows predominantly in tensile mode. However, when the cyclic stress has a strong compression component, as in contact fatigue and in submersible vehicles, the compressive stress suppresses tensile crack growth mode and shear growth mode can be dominant (Brown & Miller 1979, Liu 1985).

We suggest that when mode I and mode II loadings are combined, the mode of crack growth is determined by the relative values of the shear and tensile stress intensity factors. Because of the high $K_{II}$ at its tip, a normal fault starts to grow in the shear mode when the threshold $K_{II}$ value is reached. As long as the normal stress intensity factor is smaller than its threshold value, there will be no transition from the shear to the tensile mode growth.

Investigators have measured the threshold value of tensile stress intensity factor for a variety of rocks (Atkinson 1979). Most of the rocks tested were carbonates or sandstones and a representative value of $K_{I0}$ seems to be on the order of 1 MPa $m^{1/2}$. Because of the difficulty of preventing out-of-plane propagation of shear fractures in the laboratory, there are no measurements of threshold values of $K$ for shear fracture on rocks analogous to those for mode I loading. The values of $K_{II0}$ for some engineering materials are, however, available. By introducing high confining pressures and special geometrical contraints in their experiments, Davies *et al.* (1985) obtained $K_{II0} = 0.41$ MPa $m^{1/2}$ for soil-cement. Agarwal & Giare (1981) studied a reinforced epoxy composite with randomly oriented short-glass-fibre. They obtained $K_{II0}$ values in the order of 16 MPa $m^{1/2}$. They also found that the critical strain energy release rate in mode II is less than half of that in mode I or mode III and pointed out the importance of mode II fracture due to its lower critical value. Owing to low lithostatic pressure at the earth's surface, out-of-plane tensile cracking has been observed at the ends of strike-slip faults (e.g. Segall & Pollard 1983). For a normal fault propagating deep in the crust, however, $K_{II}$ increases much more rapidly than $K_I$ (cf. Fig. 3) and the out-of-plane cracking may be prevented. Measurements of $K_{II0}$ for geological material are essential to our better understanding of faulting processes.

To simulate the propagation of a normal fault, we postulate criteria for mixed-mode shear fracture as follows:

(1) shear crack extension starts at the crack tip and in a radial direction;

(2) crack extension starts in a plane along which shear stress $\sigma_{r\theta}$ is maximum;

(3) crack extension begins when mixed-mode effective shear stress intensity factor, as defined in equation (13), reaches a threshold value $K_{II0}$.

Our fracture criteria are expressed mathematically as

$$\sigma_{r\theta}(2\pi r)^{1/2} = K_I \sin(\theta/2)\cos^2(\theta/2) + K_{II}\cos(\theta/2)[1 - 3\sin^2(\theta/2)] = K_{II0} \quad (13)$$

which can be rewritten as

$$1 = (K_I/K_{II0})\sin(\theta/2)\cos^2(\theta/2) + (K_{II}/K_{II0})\cos(\theta/2)[1 - 3\sin^2(\theta/2)], \quad (14)$$

and

$$d(\sigma_{r\theta})/d\theta = K_I[\cos^3(\theta/2) - 2\cos(\theta/2)\sin^2(\theta/2)] + K_{II}[2\sin^3(\theta/2) - 7\sin(\theta/2)\cos^2(\theta/2)] = 0. \quad (15)$$

Equations (14) and (15) are the parametric equations of a general fracture initiation locus in the $K_I$–$K_{II}$ plane, shown in Fig. 5. Also, the direction of the initial fracture increment, $\theta^*$, can be found from equation (15). For

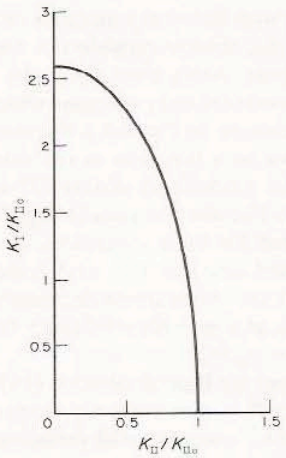


Fig. 5. Fracture initiation locus in the $K_I$–$K_{II}$ plane. When a point representing the fault tip $K_I$ and $K_{II}$ lies below the curve, the fault will not extend; on the curve, the fault grows quasistatically; above the curve, dynamic faulting is expected.

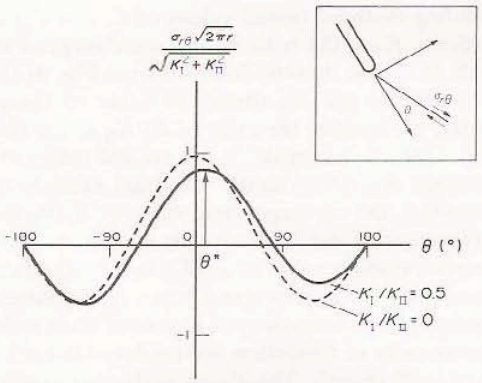


Fig. 6. Shear stresses at planes radial to the fault tip are calculated (as shown in inset). The angle $\theta$ is positive in counter-clockwise sense. The curves reveal values of the normalized shear stress as a function of the angle $\theta$. The dashed line represents the case when $K_I/K_{II}$ is 0 (pure shear mode deformation at fault tip). The solid line represents the case when $K_I/K_{II}$ equals 0.5. The orientation of the plane on which shear stress is maximum is found and denoted by $\theta^*$.

example, for pure mode II,

$$K_I = 0 \quad \text{and} \quad \theta^* = 0°$$

and the shear crack would propagate in its own plane. However, for pure mode I,

$$K_{II} = 0 \quad \text{and} \quad \theta^* = 70°.$$

That is, under pure mode I, or any combination of modes I and II, the shear crack would not propagate in its own plane.

It is worthwhile to point out that the contribution to the mixed-mode effective shear stress intensity factor comes mostly from $K_{II}$. For example, with equal value of $K_I$ and $K_{II}$, about 92% of the effective shear stress intensity factor comes from $K_{II}$ and the rest comes from $K_I$. Due to the predominance of the mode II stress intensity at a normal fault tip (Figs. 3 and 4), the difference between $K_{II}$ and effective shear stress intensity factor is negligible in practice.

An example of shear stress at planes radial to a fault tip is shown in Fig. 6. We have defined angle $\theta$ positive in counter-clockwise sense. The variation of $\sigma_{r\theta}$, normalized by $(K_I^2 + K_{II}^2)^{1/2}/(2\pi r)^{1/2}$, is shown as a function of $\theta$. As can be seen, the plane in which shear stress reaches its maximum value depends solely on the ratio $K_I/K_{II}$. If $K_I/K_{II} = 0$ (pure mode II stress), the shear stress reaches its maximum value at its original plane ($\theta = 0$) as shown by the dashed line in Fig. 6. However, as $K_I/K_{II}$ increases, the angle becomes positive, indicating that the maximum shear stress is reached at a plane shallower than the original fault plane. For this reason a listric normal fault might form.

The stress concentration in the immediate vicinity of the crack tip causes a local plastic zone. At distances large compared to the plastic zone but still small compared to the crack length, the crack tip elastic singularity dominates the stress and strain distribution. The stress distributions in this $K$-dominant field have been given by equation (12). Using the deformation theory of plasticity with stress proportional to the $n$th power of strain, Shih (1974) obtained numerical solutions for the stress distribution inside the plastic zone. The angle between the plane of maximum shear stress and the original fault plane ($\theta^*$) calculated using Shih's numerical solutions are plotted in Fig. 7 for $n = 1$ (elastic), 3 and 13. As can be seen, the more plastic (larger $n$ value) the material, the larger the angle $\theta^*$. This suggests that a listric normal fault is more likely to develop in a crust material with high degree of plasticity. For a given rheology, the larger the value of $K_I/K_{II}$, the larger the angle $\theta^*$.

We have just shown that the orientation of the shear fracture extension depends on the ratio of $K_I$ and $K_{II}$. In the last section we have also shown that this ratio depends on the surface condition and physical processes at the fault tip. For example, with a large amount of

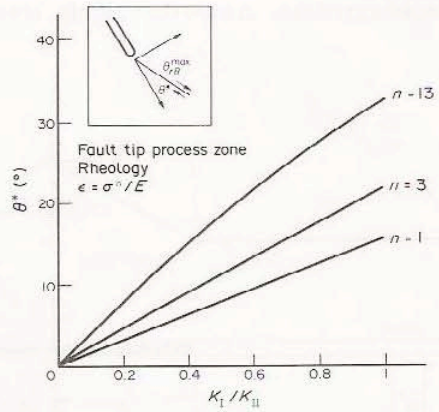


Fig. 7. $\theta^*$ denotes the angle between the plane with maximum shear stress and the original fault plane (shown in inset). The rheology of the fault tip process zone is described by the shown power law. Curves reveal the dependence of angle $\theta^*$ on the value of $K_I/K_{II}$ for $n = 1, 3$ and 13 respectively.

fault-filling material (small values of $C_s$ and $C_n$) significant $K_I$ and $K_{II}$ at the fault tip are expected prior to fault growth. It can be directly inferred from Fig. 4(a) & (b) that the larger the $K_{II}$ threshold value of the crustal material, the smaller the ratio of $K_I/K_{II}$ at the fault tip. In Fig. 4(a), for example, if the crustal material has a normalized $K_{II0}$ of 0.6 so that the fault extends at a $K_{II}$ value of 0.6, the corresponding value of $K_I/K_{II}$ is about 0.1. However, if the fault extends at a $K_{II}$ value of 0.2, the corresponding value of $K_I/K_{II}$ is 0.2. The fault will deviate more from its original plane in the latter case. The propagation trajectory of a normal fault is decided by the amount of deflection accumulated in each increment of fault growth. The above analysis suggests that a fault forming in a crustal material with large $K_{II0}$ value is less likely to become listric. On the other hand, a fault forming in a low $K_{II0}$ material is more likely to become listric. It is plausible that in a tectonic domain such as the Basin and Range Province, the abnormally high heat flow and extensive fractures of the past have either reduced the threshold value of the shear stress intensity factor or increased the plasticity of the crustal material. Both effects make listric normal faulting more likely.

## COHESIVE FORCE MODEL AND FAULT TIP BREAKDOWN ZONE

The microstructural processes of breakdown near a normal fault tip can be included directly by assuming that they give rise to cohesive forces in a zone ahead of the fault tip. These forces oppose the action of the applied loads so as to eliminate the fault tip singularity. We will apply the cohesive force model of Rice & Simons (1976) to normal faulting.

The model is shown schematically in Fig. 8(a). $D_s(x)$ is the relative shear displacement, or shear displacement-discontinuity, across the fault surface. $\sigma_s$ is the shear stress on the fault. Away from the tip breakdown zone $\sigma_s$ becomes the residual friction stress $\sigma_f$. For an inclined normal fault in the crust, this residual friction stress increases gradually toward the fault tip. However, by comparison with the sharp increase of shear stress in the end zone, the change outside the end zone is negligible. The shear stress rises to $\sigma_p$ in the end zone because of microstructural processes which cause resistance to slip initiation. In Fig. 8(b), the stress on the fault surface is shown as a function of the relative displacement $D_s(x)$. An amount of sliding $D_s^*$ is necessary to reduce $\sigma_p$ to $\sigma_f$. The shaded area in Fig. 8(b) represents the driving force for fault extension. If shear stress is constant (dashed line) in the end zone, this area is $(\sigma_p - \sigma_f)D_s^*$. If the shear stress decreases linearly from $\sigma_p$ at $x = 0$ to $\sigma_f$ at $x = -R$ (solid line), then the shaded area is $0.5\,(\sigma_p - \sigma_f)D_s^*$.

As pointed out by Rice & Simons (1976), the breakdown zone size $R$ is generally not known *a priori*. If, however, the end zone is small (small-scale yielding), then its length can be determined by requiring that the cohesive forces cancel the singular elastic stress that would be caused by the applied loads in the absence of the end zone. Theoretical studies of Palmer & Rice (1973) and Rice & Simons (1976) revealed that in the case of constant end zone stress the size of the breakdown zone $R$ can be expressed in terms of $D_s^*$:

$$R = \pi G D_s^* [4(\sigma_p - \sigma_f)(1 - \nu)]^{-1}, \qquad (16)$$

where $G$ is the shear modulus and $\nu$ Poisson's ratio. For the case of a linear decrease of stress in the end zone, the right-hand side of equation (16) should be multiplied by 9/8. In all the studies, the most uncertain of the parameters is $D_s^*$.

The end zone size $R$ for a consolidated soil has been estimated by Palmer & Rice (1973) to be in the order of 1–10 m. Rice (1979) has inferred values of $D_s^* = 2.5$ mm from data of Coulson (1972) on a natural joint in coarse-grained granite and $D_s^* = 2.5\ \mu$m from Dieterich's (1979) sliding experiments on flat ground specimens of granite. These yield $R = 1$ m and 11 mm, respectively. Rudnicki (1979), however, has suggested, based on observations of Barton (1971), that larger values of $D_s^*$, for instance, on the order of centimeters, may be more representative of *in situ* conditions. If $D_s^* = 2.5$ cm, $R = 110$ m.

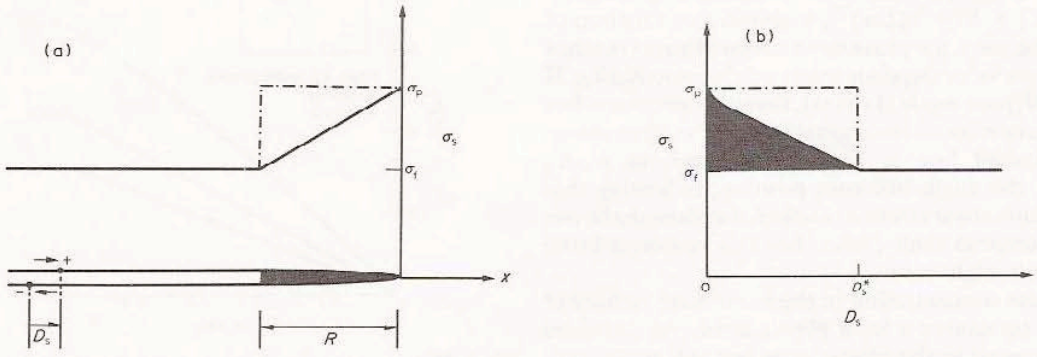


Fig. 8. Fault tip cohesive zone. (a) Away from the fault tip the residual friction stress $\sigma_f$ only varies slightly. Shear stress increases dramatically inside the cohesive zone (shaded area). (b) Shear stress plotted as a function of shear displacement-discontinuity. A $D_s^*$ value is required to reduce shear stress from $\sigma_p$ to $\sigma_f$. The shaded area represents a driving force for fault extension.

For a value of $R$ on the order of 100 m, as suggested by Rudnicki's study, the small-scale yielding condition is satisfied since the length of a macroscopic normal fault could be several km. Obviously the parameter $D_s^*$ depends strongly on conditions at the fault surface, e.g. the nature of asperity contacts, grain size, pore pressure, etc. Despite the evident importance of this size effect in extrapolating friction experiments to *in situ* conditions, there have been relatively few investigations of the precise variation of frictional stress for small values of the relative offset.

The deformation observed in the material adjacent to a fault, commonly termed fault drag, may occur within a fault tip plastic zone. If so the width of this deformed zone may give an indication of the size of the fault tip plastic zone.

## PROPAGATION OF NORMAL FAULTS IN THE CRUST

In this section we will discuss some aspects of normal fault propagation in the earth's crust. We will first consider a fault which begins in the middle of the crust and determine whether the fault will propagate upward or downward. We will then study the propagation trajectory of a normal fault. The maximum depth of a normal fault will be determined based on fracture mechanics criteria.

Study of the 1983 Borah Peak, Idaho, earthquake, and other earthquakes in the Basin and Range Province (Stein & Barrientos 1985) reveals that the mainshocks in this region usually nucleate at mid-crustal depth of 15 km and along moderate, 45–65° dipping fault zones. Aftershocks of the earthquakes are clearly distributed above the depths of the mainshock focus and the mainshock/aftershock distributions sometimes extend laterally beyond the surface faulting.

The upward migration of earthquake rupture has also been suggested for the earthquakes at mid-ocean ridges (Huang *et al.* 1986). For the median valley near 23°N at the Mid-Atlantic Ridge, there is a difference in depth between the slip zones of the large earthquakes (mean depth of 1.5–2.5 km) and the regions of most intense microearthquake activity (5–8 km) (Toomey *et al.* 1985). To explain this difference in depth, Huang and others suggest that microearthquakes in the median valley outline a strong portion of the crust between 1–2 and 5–6 km depth and that fault rupture during large earthquakes begins near the base of the crust and propagates upward to the seafloor. The microearthquake focal depths provide a measure of the maximum depth of brittle behavior of the crust. It is therefore of interest to study the case where a normal fault is initiated by a weakness (pre-existing crack) both of whose ends are inside the earth's crust (see the inset of Fig. 9a).

We have calculated the stress intensity factors at both ends of the fault (Fig. 9). It can be seen that if the far field loading is independent of depth, the shear stress intensity factor at the lower tip is smaller than that at the upper tip (Fig. 9a). This is due to the large lithostatic stress at the lower tip. With the same applied stress the lower end of the fault is more difficult to slide. However, after the fault has propagated to the free surface, the shear stress will start to concentrate more on the lower tip and the fault will eventually propagate downward as the far field stress increases. On the other hand, if the far field loading increases linearly with depth, $K_{II}$ on the lower tip becomes slightly larger than that at the upper tip (Fig. 10a), and the normal fault is most likely to propagate from the lower end.

Up to now we have only addressed the problem of predicting normal fault extension immediately at the end(s) of a pre-existing weakness (crack). It is certainly of interest to study the incremental growth of a normal fault: where it goes, what it does along the way, and how much energy it takes to get there.

We have shown how to compute stress intensities, and how to use them to predict the direction of the next incremental fault. To complete our fracture propagation model we must also be able to predict either (a) the length of a fracture increment for a given load or (b) the

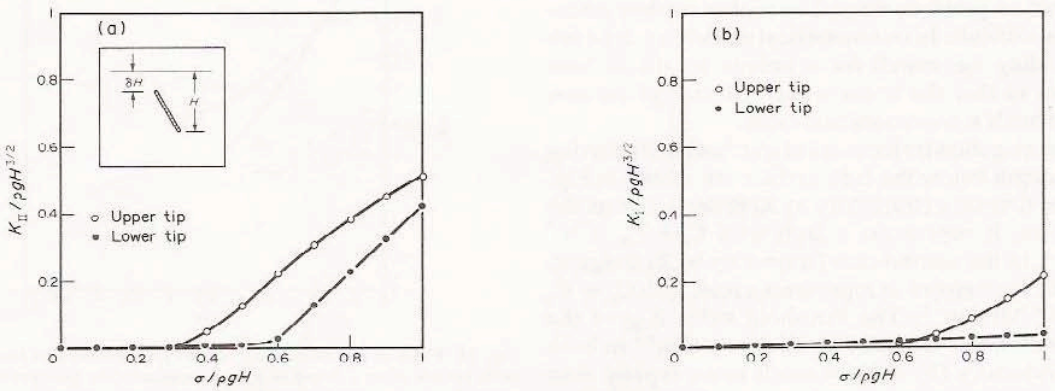


Fig. 9. Inset shows a fault segment with its upper end at depth $\delta H$ and lower end at depth $H$. Comparison of $K_{II}$(a) and $K_I$(b) at the upper and lower ends of the fault segment when far field loading is independent of depth. $C_s$ and $C_n$ are the same as in Fig. 3(a). Notice that $K_{II}$ at the upper end is greater than that at the lower end.

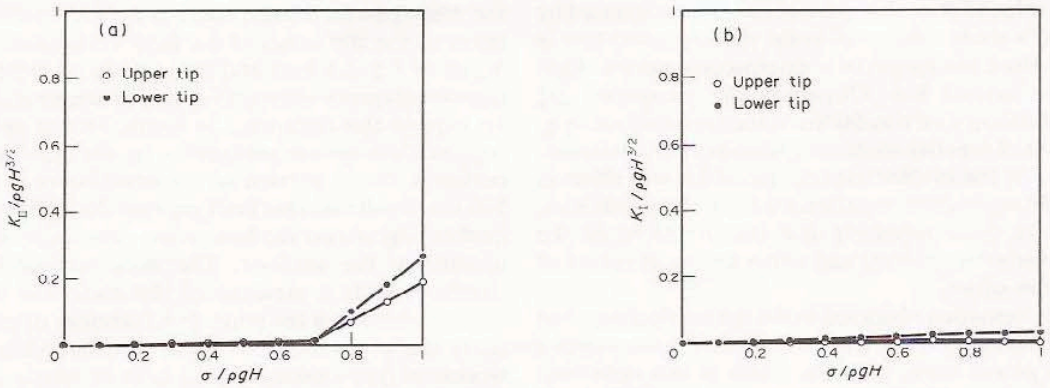


Fig. 10. Similar to Fig. 9(a) and (b), but in this case the far field loading increases linearly with depth. $C_s$ and $C_n$ are the same as in Fig. 3(a). Both $K_{II}$ and $K_I$ show greater values at the lower end than the upper end.

load change required to drive a fault a specified length. In the following we will examine the incremental propagation of a normal fault in response to given load change.

The fundamental principle here is that a fracture, once initiated, will continue to propagate as long as there is sufficient energy or, equivalently, effective shear stress intensity, available. Effective shear stress intensity refers to a mixed-mode case and is the combination of mode I and mode II stress intensity factors as described before (equation 14). As we have also mentioned before, the difference between $K_{II}$ and the effective shear stress intensity factor is negligible in practice. In our numerical modelling, the effective shear stress intensity factor at the fault tip (calculated at the end of the most recently added element) is required to match a constant threshold value $K_{II0}$ and the normal and shear stresses on the newly formed fault segments are required to obey the frictional sliding law as given by the strength envelopes in Fig. 2(a).

An important aspect of normal fault propagation is that, for a given tensile loading, the effective shear stress intensity factor decreases with increasing fault length. This is a direct consequence of an increase in frictional force on the fault. As a normal fault extends to great depth, the frictional stress on each new fault segment is larger than on previous ones. This makes further extension more difficult. In our numerical modelling, for each given loading we search for a unique length of fault increment so that the stress intensity factor at the new fault tip equals a given constant value.

Two propagation trajectories of a normal fault starting at 5 km depth below the free surface are shown in Fig. 11. In the first case (trajectory a) $K_I$ is negligible as the fault grows. It represents a fault with $C_s = C_n = 10^5$ MPa m$^{-1}$. In the second case (trajectory b) $K_I$ is significant as the fault grows. It represents a fault with $C_s = C_n = 2 \times 10^4$ MPa m$^{-1}$. The threshold value $K_{II0}$ of the crustal material is assumed to be $3 \times 10^3$ m$^{1/2}$ in both cases. Trajectory (b) flattens much more rapidly than trajectory (a), consistent with our earlier prediction based on the analysis of $K_I/K_{II}$ at a fault tip. Our numerical solutions also confirm that when a normal fault propagates in a crustal material with a low $K_{II0}$, it becomes more listric than it would be in a crustal material with a high $K_{II0}$.

In general, for the same incremental increase in far field loading, the length of the newly formed fault increment decreases as the fault propagates to greater depth (Fig. 12), reflecting greater frictional resistance to sliding. For a prescribed far field loading, there is an equilibrium depth for the fault tip. This equilibrium depth is plotted in Fig. 13 for three values of threshold shear stress intensity factor—$0.9 \times 10^3$, $3 \times 10^3$ and $4.5 \times 10^3$ MPa m$^{1/2}$. As can be seen, a normal fault will grow to a greater depth in a crustal material with lower threshold value (weak material) than it would in a material with higher threshold value (strong material).

It is worthwhile to point out the important differences between a friction-free shear crack and a shear crack whose frictional stress increases toward one end. For a friction-free crack, the shear stress intensity factor increases with crack length. If the far field loading is kept constant, the propagation of the crack will eventually become unstable. The stress intensity factor for a shear

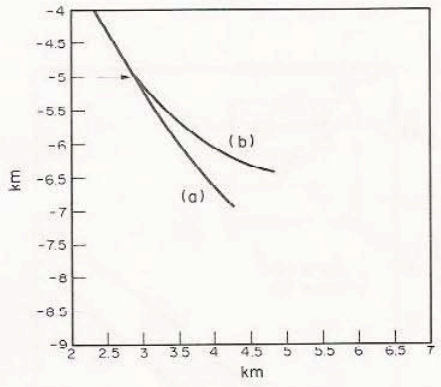


Fig. 11. Fault propagation trajectories for two normal faults. They both initiate from a depth of 5 km as indicated by the arrow. In both cases $K_{II0} = 3 \times 10^3$ MPa m$^{1/2}$. Trajectory (a): $C_s = C_n = 10^5$ MPa m$^{-1}$, representing negligible $K_I$ at fault tip as fault grows. Trajectory (b): $C_s = C_n = 2 \times 10^4$ MPa m$^{-1}$, representing significant $K_I$ at fault tip as fault grows.

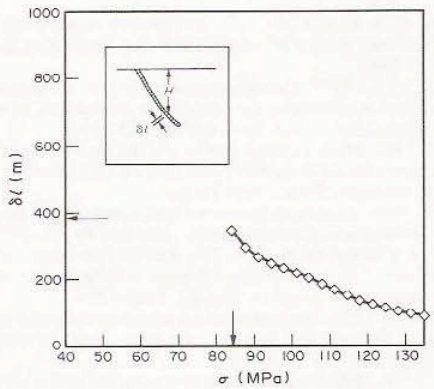


Fig. 12. A normal fault incrementally grows from the end of a pre-existing crack (inset). $\sigma$ is the magnitude of far field loading. $\delta l$ is the predicted length of the new fault segment. Notice that the load change in each increment is constant. In this calculation, $K_{II0}$ is assumed to be $3 \times 10^3$ MPa $m^{1/2}$, and the fault begins at a depth of 5 km. Discrete boundary elements on the pre-existing crack have a length indicated by the horizontal arrow. Fault extension starts to occur at a far field loading indicated by the vertical arrow. As the fault propagates to greater depth (corresponding to larger value of far field loading), the length of the new fault segment decreases.

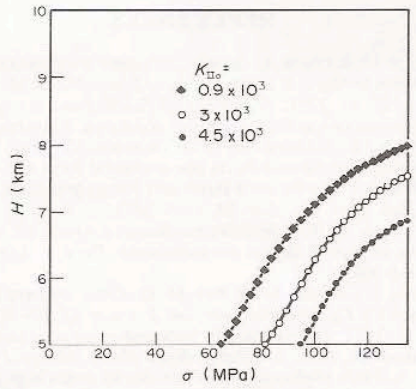


Fig. 13. The equilibrium depth $H$ of normal faults (cf. the inset of Fig. 12) forming in crustal materials with three values of $K_{II0}$. $\sigma$ is the magnitude of far field loading. All the faults are assumed to begin at a depth of 5 km. In all cases $C_n$ and $C_s$ are the same as Fig. 4(a). Filled diamond: $K_{II0} = 0.9 \times 10^3$ Mpa $m^{1/2}$. Open circle: $K_{II0} = 3 \times 10^3$ Mpa $m^{1/2}$. Filled circle: $K_{II0} = 4.5 \times 10^3$ Mpa $m^{1/2}$. For a given far field loading, a normal fault grows to greater depth in a material with lower $K_{II0}$.

crack with constant surface frictional stress also increases with length, although its magnitude is proportionally smaller than that of a friction-free crack. A normal fault is different from these two types of shear crack: its frictional stress increases toward the lower tip, which makes the downward propagation stable.

For a normal fault quasistatically propagating in an elastic half space, both shear and normal displacement-discontinuities decrease to zero as the fault tip is approached. If far field loading is small at the surface and increases with depth, the predicted normal displacement-discontinuity is small everywhere on a normal fault. A substantial normal opening at the surface is, however, predicted for a normal fault under a far field loading which is independent of depth. The predicted opening is even more substantial for a listric normal fault. In these cases it is likely that, owing to the effect of gravitational forces, failure will occur in the hangingwall block by antithetic normal faults which are conjugate to the main normal fault. Such antithetic normal faults are commonly observed in extensional environments (Wernicke & Burchfiel 1982, Anderson *et al.* 1983). Surface deformations in the vicinity of a main normal fault are then the contributions from the dislocations on both the main and secondary normal faults. The horizontal extent of the secondary normal faults is related to the mode of far field loading and the geometry of a main fault, therefore their presence could provide constraints on the structure of a main fault.

## CONCLUSIONS

We have developed a model for normal fault propagation in which the fault, as a shear crack in the earth's crust, propagates in response to a stress concentration at its tip. Our analysis reveals that the shear stress intensity at the tip of a deep normal fault dominates the tensile stress intensity, suggesting that out-of-plane tensile cracking might be prevented. Measurement of $K_{II0}$ (shear fracture toughness) for geological material is essential to our understanding of the faulting process.

Analysis of stresses at the tip of a normal fault shows that the orientation of a plane radial to the tip along which the fault extends by shear failure depends on the ratio of $K_I$ and $K_{II}$. With a non-zero mode I stress intensity, this plane is not the original plane of shear failure. A listric normal fault is likely to form in crustal material with a relatively small shear fracture toughness. A listric normal fault is also more likely to form in crustal material with a high degree of plasticity.

We have examined the propagation trajectory of an incrementally growing normal fault. During propagation, the effective shear stress intensity factor of the normal fault is required to match the threshold value of the surrounding crustal material. As a normal fault extends to great depth, the shear stress intensity factor at the fault tip decreases. This is due to an increase in fault surface frictional stress. To make further growth possible, a larger horizontal tensile loading is required to increase the fault tip stress intensity. The equilibrium depth to which a normal fault will grow is controlled by the magnitude of the far field loading and the shear fracture toughness of the crustal material. Decrease of the shear stress intensity factor with fault length also stabilizes the fault growth and makes quasistatic propagation possible.

*Acknowledgements* This research was partially supported by NASA grant NSG 7605. Helpful discussions with Jason Phipps Morgan, Michael Blanpied, Lee Ditullio and Terry Tullis are gratefully acknowledged. Paul Segall and an anonymous reviewer provided helpful comments on an earlier version of the manuscript.

## REFERENCES


Agarwal, B. D. & Giare, G. S. 1981. Fracture toughness of short fibre composites in Mode II and III. *Engng Fract. Mech.* **15**, 219–239.

Anderson, E. M. 1951. *Dynamics of Faulting and Dyke Formation with Applications to Britain*. Oliver and Boyd, Edinburgh.

Anderson, R. E., Zoback, M. L. & Thomson, G. 1983. Implications of selected subsurface data on the structural form and evolution of some basins in the northern Basin and Range province, Nevada and Utah. *Bull. geol. Soc. Am.* **94**, 1055–1072

Atkinson, B. K. 1979. A fracture mechanics study of subcritical tensile cracking of quartz in wet environments. *Pure & Appl. Geophys.* **117**, 1011–1024.

Banks-Sills, L., Arcan, M. & Bui, H. D. 1983. Toward a pure shear specimen for $K_{II}$ determination. *Int. J. Fract.* **22**, R9–R14.

Barton, N. 1971. A relationship between joint roughness and joint shear strength. *Proc. Int. Symp. Rock Mech., Nancy*. Pap I–8.

Berg, C. A. 1965. Deformation of fine cracks under high pressure and shear. *J. geophys. Res.* **70**, 3447–3452.

Brown, M. W. & Miller, K. J. 1979. Initiation and growth of cracks in biaxial fatigue. *Fatigue Engng Mater. Struct.* **1**, 231–246.

Brun, J. P. & Choukroune, P. 1983. Normal faulting, block tilting, and decollement in a stretched crust. *Tectonics* **2**, 345–356.

Chisholm, D. B. & Jones, D. L. 1977. An analytic and experimental stress analysis of a practical mode II fracture test specimen. *Exper. Mech.* **17**, 7–13.

Chiu, S. T. & Liu, A. F. 1976. Mixed-mode fracture of shear panels—A finite element analysis. In: *Mechanics of Crack Growth*. ASTM STP 590, American Society for Testing and Materials, 263–280.

Cornet, F. H. 1979. Comparative analysis by the displacement-discontinuity method of two energy criteria of fracture. *J. appl. Mech.* **46**, 349–355.

Coulson, J. H. 1972. Shear strength of flat surfaces in rock. In: *Proc. US Symp. Rock Mech. 13th, Urbana, Il.*, 1971 (edited by Cording, E. J.), 77–105.

Crouch, S. L. & Starfield, A. M. 1983. *Boundary Element Methods in Solid Mechanics: With Applications in Rock Mechanics and Geological Engineering*. George Allen and Unwin, London.

Das, S. & Scholz, C. H. 1981. Theory of time-dependent rupture in the earth. *J. geophys. Res.* **86**, 6039–6051.

Davies, J., Morgan, T. J. & Yim, A. W. 1985. The finite element analysis of a pure-through shear specimen in mode II. *Int. J. Fract.* **28**, R3–R10.

Dieterich, J. H. 1979. Modeling of rock friction, Part I: Experimental results and constitutive equations. *J. geophys. Res.* **84**, 2161–2168.

Digby, P. J. & Murrell, S. A. F. 1975. The role of shear stress concentrations in the initiation of brittle fracture in bodies containing closed cracks. *Bull. seismo. Soc. Am.* **65**, 1163–1171.

Effimoff, I. & Pinezich, A. R. 1981. Tertiary structural development of selected valleys based on seismic data: Basin and Range province, northeastern Nevada. *Philos. Trans. Roy. Soc. London* **A300**, 435–442.

Freund, L. B. 1979. The mechanics of dynamic shear crack propagation. *J. geophys. Res.* **84**, 2199–2209.

Hafner, W. 1951. Stress distributions and faulting. *Bull. geol. Soc. Am.* **62**, 373–398.

Harper, G. D. 1985. Tectonics of slow spreading mid-ocean ridges and consequences of a variable depth to the brittle/ductile transition. *Tectonics* **4**, 395–409.

Huang, P. Y., Solomon, S. C., Bergman, E. A. & Nabelek, J. L. 1986. Focal depths and mechanisms of Mid-Atlantic Ridge earthquakes from body wave inversion. *J. geophys. Res.* **91**, 579–598.

Jackson, J. & McKenzie, D. 1983. The geometrical evolution of normal fault systems. *J. Struct. Geol.* **5**, 471–482.

Jaeger, J. C. & Cook, N. G. 1969. *Fundamentals of Rock Mechanics*. Methuen, London.

Ingraffea, A. R. 1977. Discrete fracture propagation in rock: laboratory tests and finite element analysis. Unpublished Ph.D. Thesis, University of Colorado.

Karson, J. A. 1984. Variations in extensional faulting along the Mid-Atlantic Ridge. *EOS, Trans. AGU* **65**, 1114.

Lawn, B. R. & Wilshaw, T. R. 1975. *Fracture of Brittle Solids*. Cambridge University Press, Cambridge.

Liu, H. W. 1985. Shear fatigue crack growth: a literature survey. *Fatigue Fract. Engng Mater. Struct.* **8**, 295–313.

Mills, N. S. 1981. Dislocation array elements for the analysis of crack and yielded zone growth. *J. Mater. Sci.* **16**, 1317–1331.

Muskhelishvili, N. I. 1975. *Some Basic Problems of the Mathematical Theory of Elasticity*. Noordhoff, Leyden.

Palmer, A. C. & Rice, J. R. 1973. The growth of slip surfaces in the progressive failure of over-consolidated clay. *Proc. Roy. Soc. Lond.* **A332**, 527–548.

Proffett, J. M. Jr. 1977. Cenozoic geology of the Yerington district, Nevada, and implications for the nature and origin of basin and range faulting. *Bull. Geol. Soc. Am.* **88**, 247–266.

Rice, J. R. 1968. Mathematical analysis in the mechanics of fracture. In: *Fracture: An Advanced Treatise* (edited by Liebowitz). Vol. 2, 191–311. Academic Press, New York.

Rice, J. R. 1979. Theory of precursory processes in the inception of earthquake rupture. *Gerlands Beitr. Geophys.* **88**, 91–127.

Rice, J. R. & Simons, D. A. 1976. The stabilization of spreading shear faults by coupled deformation-diffusion effects in fluid-infiltrated porous materials. *J. geophys. Res.* **81**, 5322–5334.

Rudnicki, J. W. 1979. The stabilization of slip on a narrow weakening fault zone by coupled deformation-pore fluid diffusion. *Bull. Seismo. Soc. Am.* **69**, 1011–1024.

Rudnicki, J. W. 1980. Fracture mechanics applied to the earth's crust. *Annu. Rev. Earth Planet. Sci.* **8**, 489–525.

Sanford, A. R. 1959. Analytical and experimental study of simple geological structure. *Bull. Geol. Soc. Am.* **70**, 19–51.

Scholz, C. H., Wyss, M. & Smith, S. W. 1969. Seismic and aseismic slip on the San Andreas Fault. *J. geophys. Res.* **74**, 2049–2069.

Segall, P. & Pollard, D. D. 1983. Nucleation and growth of strike slip faults in granite. *J. geophys. Res.* **88**, 555–568.

Shih, C. F. 1974. Small-scale yielding analysis of mixed mode plane-strain crack problems. In: *Fracture Analysis*. ASTM STP 560, American Society for Testing and Materials, 187–210.

Stein, R. S. & Barrientos, S. E. 1985. Planar high-angle normal-faulting in the Basin and Range: Geodetic analysis of the 1983 Borah Peak, Idaho, earthquake. *J. geophys. Res.* **90**, 11355–11366.

Stewart, J. H. 1970. Basin-range structure in western North America; A review. *Mem. geol. Soc. Am.* **152**, 1–31.

Toomey, D. R., Solomon, S. C., Purdy, G. M. & Murrey, M. H. 1985. Microearthquakes beneath the median valley of the Mid-Atlantic Ridge near 23°N: Hypocenters and focal mechanisms. *J. geophys. Res.* **90**, 5443–5458.

Wernicke, B. 1985. Uniform-sense normal simple shear of the continental lithosphere. *Can. J. Earth Sci.* **22**, 108–125.

Wernicke, B. & Burchfiel, B. C. 1982. Modes of extensional tectonics. *J. Struct. Geol.* **4**, 105–115.


## APPENDIX

In this section two-dimensional linear elastic theory is used to derive the Green's functions for a crack element in an elastic half plane with a stress free surface. We will first develop the Green's functions for a single dislocation and then superimpose or integrate these solutions to obtain the Green's functions for a constant displacement element and a crack tip element for which displacement discontinuity varies as a square root function of the distance from one end.

Displacement and stress are represented in terms of analytic functions $\phi(Z)$ and $\psi(Z)$ of the complex variable $Z = x + iy$:

$$\tfrac{1}{2}(\sigma_{yy} + \sigma_{xx}) = 2\,\mathrm{Re}\,\phi'(Z) \tag{A1}$$

$$\tfrac{1}{2}(\sigma_{yy} - \sigma_{xx} + 2i\sigma_{xy}) = \bar{Z}\phi''(Z) + \psi'(Z) \tag{A2}$$

$$2G(u_x + iu_y) = \varkappa\phi(Z) - Z\overline{\phi'(Z)} - \overline{\psi(Z)} \tag{A3}$$

where $G$ is shear modulus and $\varkappa$ equals to $3 - 4\nu$, where $\nu$ is Poisson's ratio. Primes denote differentiates with respect to $Z$, and the bars indicate complex conjugation.

The stress functions for an edge dislocation at a point $Z_d$ in an infinite elastic plane are given by

$$\phi_d(Z) = \gamma_d \ln[(Z - Z_d)/T] \tag{A4}$$

$$\psi_d(Z) = \overline{\gamma_d} \ln[(Z - Z_d)/T] + \gamma_d Z_d/(Z - Z_d) \tag{A5}$$

where $\gamma_d$ is the complex Burger's vector representing the magnitude of the dislocation and $T = e^{i\theta}$ is the direction along which the function $\ln[(Z - Z_d)/T]$ has its branch cut (see Fig. A1).

Using the method of analytic continuation across the $y$-axis (Mills 1981), the stress functions in the half-plane that will give $\sigma_{yy} = \sigma_{xy} = 0$ on the $y$-axis are

$$\phi(Z) = \phi_d(Z) - Z\overline{\phi'_d(\bar{Z})} - \overline{\psi_d(\bar{Z})} \tag{A6}$$

$$\psi(Z) = \psi_d(Z) + Z\overline{\psi'_d(\bar{Z})} - \overline{\phi_d(\bar{Z})} + Z^2\overline{\phi''_d(\bar{Z})}\,. \tag{A7}$$

When equations (A4) and (A5) are substituted in equations (A6) and (A7) respectively, and the stress and displacement components evaluated using equations (A1), (A2) and (A3), the results are

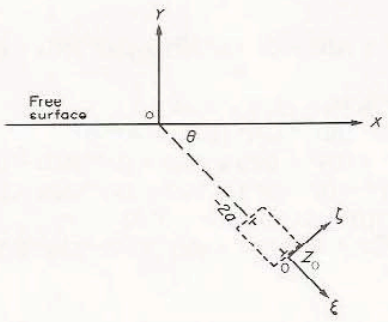


Fig. A1. A constant displacement element is shown in an elastic half-plane. The element comprises two dislocations which lie on a line (dashed line) making an angle $\theta$ with the free surface. A local coordinate system ($\xi$, $\zeta$) is introduced with its origin at point $Z_0$.

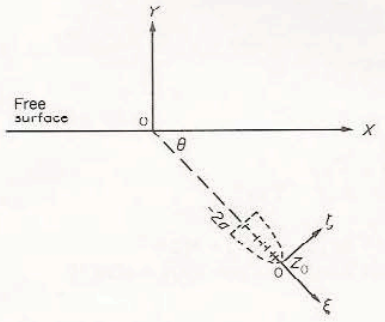


Fig. A2. A crack tip element is located in an elastic half-plane. The displacement discontinuity is zero at the crack tip and builds up as a square root function to $\sqrt{2}(b_x + ib_y)$ at $\xi = -2a$. The corresponding dislocation density is given in equation (A11).

$$\tfrac{1}{2}(\sigma_{yy} + \sigma_{xx}) = 2\,\mathrm{Re}\,\{\gamma_d/(Z - Z_d) - \gamma_d/(Z - \bar{Z}_d) + \bar{\gamma}_d(\bar{Z}_d - Z_d)/(Z_d - \bar{Z}_d)^2\} \quad \text{(A8)}$$

$$\tfrac{1}{2}(\sigma_{yy} - \sigma_{xx} + 2i\sigma_{xy}) = \{-\gamma_d(\bar{Z} - \bar{Z}_d)/(Z - Z_d)^2 + \bar{\gamma}_d/(Z - Z_d)\} + \{\gamma_d(\bar{Z} - \bar{Z}_d)/(Z - \bar{Z}_d)^2 - \bar{\gamma}_d/(Z - \bar{Z}_d)\} + \{\gamma_d(Z_d - \bar{Z}_d)(2Z - Z - \bar{Z}_d)/(Z - \bar{Z}_d)^3\} \quad \text{(A9)}$$

$$2G(u_x + iu_y) = \{\kappa\gamma_d \ln[(Z - Z_d)/T] - \gamma_d \overline{\ln[(Z - Z_d)/T]} - \bar{\gamma}_d(Z - Z_d)/(\bar{Z} - \bar{Z}_d)\} + \{-\kappa\gamma_d \overline{\ln[(Z - Z_d)/T]} + \gamma_d \ln[(\bar{Z} - Z_d)/T] + \bar{\gamma}_d(Z - Z_d)/(\bar{Z} - Z_d)\} + \{+\kappa\bar{\gamma}_d(Z_d - \bar{Z}_d)/(Z - \bar{Z}_d) + \gamma_d(Z - \bar{Z})(Z_d - \bar{Z}_d)/(\bar{Z} - Z_d)^2 - 4\bar{\gamma}_d(1 - \nu)\}. \quad \text{(A10)}$$

To study the stress functions of a constant displacement element and a crack tip element with square root displacement variation, we have introduced a local coordinate system ($\xi$, $\zeta$) as shown in Fig. A1. The origin of this local coordinate system is chosen at the tip of the element $Z_0$ and the $\xi$ axis is chosen to coincide with the element orientation $T = e^{i\theta}$.

*Constant displacement element*

For a constant displacement element a displacement discontinuity of magnitude $b_x + ib_y$ occurs along the $\xi$-axis from $-2a$ to 0 (Fig. A1). The element can be made up of a dislocation of magnitude $\gamma$ ending at $\xi = -2a$, and a dislocation of magnitude $-\gamma$ ending at $\xi = 0$, where $\gamma = G(b_x + ib_y)/4i\pi(1 - \nu)$. Therefore the Green's functions of the constant displacement element are obtained by the summation of the following two solutions

(1) solutions of equations (A8)–(A10) with $\gamma_d = +\gamma$ and $Z_d = Z_0 - 2aT$
(2) solutions of equations (A8)–(A10) with $\gamma_d = -\gamma$ and $Z_d = Z_0$.

*Crack tip element*

A crack tip element with its tip at $\xi = 0$ is shown in Fig. A2. The displacement discontinuity is zero at the crack tip and builds up as a square root function to $\sqrt{2}(b_x + ib_y)$ at $\xi = -2a$. The displacement discontinuity at the center of the element ($\xi = -a$) is therefore $(b_x + ib_y)$. We again denote $\gamma = G(b_x + ib_y)/4i\pi(1 - \nu)$. This element can be made up of a dislocation of magnitude $\sqrt{2}\gamma$ ending at $\xi = -2a$, and a series of dislocations with magnitude $-\gamma$ distributed from $\xi = -2a$ to 0. The dislocation density is given by (Mills 1981)

$$\varrho(\xi) = \begin{cases} 1/(-\xi)^{1/2} & \text{for } 0 > \xi > -2a \\ 0 & \text{for } \xi < -2a \text{ or } \xi > 0. \end{cases} \quad \text{(A11)}$$

The Green's functions of such a crack tip element comprises contributions from each distributed dislocation. More specifically we can obtain them by adding the following two solutions:

(1) solutions of equations (A8)–(A10) with $\gamma_d = \sqrt{2}\gamma$ and $Z_d = Z_0 - 2aT$

(2) solutions from the integration of equations (A8) (A10) with $\gamma_d = -\gamma$. The integration is done from $\xi = -2a$ to 0 using the dislocation density given by equation (A11). In the following expressions we denote

$$G = (2\bar{Z} - Z - \bar{Z}_0)/\bar{T}$$
$$H = (\bar{Z}_0 - Z_0)/(\bar{T} - T)$$
$$Q1 = [(Z_0 - Z)/T]^{1/2}$$
$$Q2 = [(\bar{Z}_0 - Z)/T]^{1/2}.$$

After some algebraical operations the integrations give the stresses and displacements as follows:

$$\tfrac{1}{2}(\sigma_{yy} + \sigma_{xx}) - 2\,\mathrm{Re}\left\{\sum_{i=1}^{3} A_i B_i\right\} \quad \text{(A12)}$$

where

$$A1 = \gamma/T$$
$$A2 = -\gamma/\bar{T}$$
$$A3 = \bar{\gamma}(\bar{T} - T)/\bar{T}^2$$
$$B1 = -\ln\{[Q1 + (2a)^{1/2}]/[Q1 - (2a)^{1/2}]\}/Q1$$
$$B2 = -\ln\{[Q2 + (2a)^{1/2}]/[Q2 - (2a)^{1/2}]\}/Q2$$
$$B3 = (H/Q2^2 + 1)\ln\{[Q2 + (2a)^{1/2}]/[Q2 - (2a)^{1/2}]\}/(2Q2) + (2a)^{1/2}(H/Q2^2 - 1)/(Q2^2 - 2a)$$

$$\tfrac{1}{2}(\sigma_{yy} - \sigma_{xx} + 2i\sigma_{xy}) = \left\{\sum_{i=1}^{5} C_i D_i\right\} \quad \text{(A13)}$$

where

$$C1 = -\gamma\bar{T}/T^2$$
$$C2 = \bar{\gamma}/T$$
$$C3 = \gamma/\bar{T}$$
$$C4 = -\bar{\gamma}/\bar{T}$$
$$C5 = \bar{\gamma}(T - T)/\bar{T}^2$$
$$D1 = (\bar{Q}1^2/Q1^2 + 1)\ln\{[Q1 + (2a)^{1/2}]/[Q1 - (2a)^{1/2}]\}/(2Q1) + (2a)^{1/2}(\bar{Q}1^2/Q1^2 - 1)/(2a - Q1^2)$$
$$D2 = -\ln\{[Q1 + (2a)^{1/2}]/[Q1 - (2a)^{1/2}]\}/Q1$$
$$D3 = -(\bar{Q}1^2/Q2^2 + 1)\ln\{[Q2 + (2a)^{1/2}]/[Q2 - (2a)^{1/2}]\}/(2Q2) + (2a)^{1/2}(\bar{Q}1^2/Q2^2 - 1)/(2a - Q2^2)$$
$$D4 = -\ln\{[Q2 + (2a)^{1/2}]/[Q2 - (2a)^{1/2}]\}/Q2$$
$$D5 = \{-3(Q2^2 + G)(-Q2^2 + H)/(8Q2^4) + (-2Q2^2 - G + H)/(2Q2^2) + 1\} \times \ln\{[Q2 + (2a)^{1/2}]/[Q2 - (2a)^{1/2}]\}/Q2 - (2a)^{1/2}(5Q2^2 - 6a)(Q2^2 + G) \times (-Q2^2 + H)/[4Q2^4(Q2^2 - 2a)^2] + (2a)^{1/2}(-2Q2^2 - G + H))/[Q2^2(Q2^2 - 2a)]$$

$$2G(u_x + iu_y) = \left\{\sum_{i=1}^{9} E_i F_i\right\} \quad \text{(A14)}$$

where

$$E1 = \kappa\gamma$$
$$E2 = -\gamma$$
$$E3 = -\overline{\gamma}I/\overline{T}$$
$$E4 = -\kappa\gamma$$
$$E5 = \gamma$$
$$E6 = \overline{\gamma}$$
$$E7 = \kappa\overline{\gamma}(T - \overline{T})/\overline{T}$$
$$E8 = \gamma(\overline{Z} - Z)(T - \overline{T})/T^2$$
$$E9 = -4\overline{\gamma}(1 - \nu)$$
$$F1 = 2(2a)^{1/2} \ln \{2a - Q1^2\} - 4(2a)^{1/2} + 2Q1 \ln \{[Q1 + (2a)^{1/2}]/[Q1 - (2a)^{1/2}]\}$$
$$F2 = \overline{F}1$$
$$F3 = 2(2a)^{1/2} + (Q1^2 - \overline{Q}1^2) \ln \{[\overline{Q}1 + (2a)^{1/2}]/[\overline{Q}1 - (2a)^{1/2}]\}/\overline{Q}1$$
$$F4 = \overline{F}5$$
$$F5 = 2(2a)^{1/2} \ln \{2a - \overline{Q}2^2\} - 4(2a)^{1/2} + 2\overline{Q}2 \ln \{[\overline{Q}2 + (2a)^{1/2}]/[\overline{Q}2 - (2a)^{1/2}]\}$$
$$F6 = 2(2a)^{1/2} + (Q1^2 - \overline{Q}2^2) \ln \{[\overline{Q}2 + (2a)^{1/2}]/[\overline{Q}2 - (2a)^{1/2}]\}/\overline{Q}2$$
$$F7 = -2(2a)^{1/2} - (H - Q2^2) \ln \{[Q2 + (2a)^{1/2}]/[Q2 - (2a)^{1/2}]\}/Q2$$
$$F8 = -(2a)^{1/2}(H - \overline{Q}2^2)/[\overline{Q}2^2(2a - \overline{Q}2^2)] + (H/\overline{Q}2^2 + 2) \ln \{[\overline{Q}2 + (2a)^{1/2}]/[\overline{Q}2 - (2a)^{1/2}]\}/(2\overline{Q}2)$$
$$F9 = 2(2a)^{1/2}.$$